Modeling Physical Processes in CAMILA Hall Thruster by PIC Method

IEPC-2011-043

Presented at the 32nd International Electric Propulsion Conference, Wiesbaden, Germany September 11–15, 2011

Igal Kronhaus*
Faculty of Aerospace Engineering, Technion - Israel Institute of Technology, Haifa 32000, Israel

Alexander Kapulkin†
Asher Space Research Institute, Technion - Israel Institute of Technology, Haifa 32805, Israel

Moshe Guelman‡
Faculty of Aerospace Engineering, Technion - Israel Institute of Technology, Haifa 32000, Israel

and

Benveniste Natan§
Faculty of Aerospace Engineering, Technion - Israel Institute of Technology, Haifa 32000, Israel

Abstract: The CAMILA concept was introduced to improve the ionization efficiency in low power Hall thrusters. With relatively large coaxial anode surfaces and longitudinal magnetic strength, the CAMILA represents a significant departure from conventional Hall thrusters. In order to investigate the physical processes inside the CAMILA thruster, a two dimensional simulation of the thruster channel is used. Two magnetic configurations are analyzed: simplified CAMILA with conventional magnetic field and full CAMILA with strengthened longitudinal component of the magnetic field. The simulation is fully kinetic with the electrons, ions and gas atoms (Xenon) represented as particles. Electron-neutral interaction are included together with particle-boundary interactions such as recombination and secondary emission. In addition, dielectric boundaries are floating and the cathode is represented as a free-space boundary, emitting electrons to satisfy quasi-neutrality on its surface. The high anode efficiency, observed in experiments, can be attributed to several mechanisms that were found in the presented work. In the simplified case, a focusing potential is created near the anode-dielectric boundary that directs ions away from the walls. It is created because of the placement of the anodes, in parallel with the channel, and the penetration of plasma inside the anode cavity. In the full CAMILA case, electron attracting regions are established inside the anode cavity. In these regions, electrons are heated sufficiently to reach high a degree of ionization inside the anode cavity, while ion currents to the anode surfaces are reduced significantly.

* Ph.D. Student, igalkron@tx.technion.ac.il.
† Senior Scientist, Head, Electric Propulsion Laboratory, kapulkin@tx.technion.ac.il.
‡ Professor Emeritus, aerglmn@aerodyne.technion.ac.il.
§ Associate Professor, Head, Missile Propulsion Laboratory, aerbeny@aerodyne.technion.ac.il.

Nomenclature

a_c = thermal accommodation coefficient
$\vec{B}$ = magnetic field
$\vec{E}$ = electric field
F_i = incident energy flux
F_r = reflected energy flux
F_w = full accommodation energy flux
I_d = discharge current
m = particle mass
N_c = number of macro-particle collisions
N_e = total number of electron macro-particles
n = plasma density
n_a = Xenon atom (XeI) density
P_{null} = null probability for collisions
$< Q_{eai} V_e >$ = electron-XeI ionization reaction rate
q = particle charge
R = ionization rate
r = radial coordinate
t = time
$\vec{V}$ = particle velocity
V_e = electron velocity magnitude
$V_{e\theta}$ = azimuthal electron velocity
$V_{e\perp}$ = electron velocity perpendicular to the magnetic field and azimuthal directions
$\vec{x}$ = particle position
z = axial coordinate
Δt = electron time step
ϵ = dielectric permittivity
ε = particle energy
λ_D = Debye length
ν_{max} = maximal collision frequency
ρ = charge density
σ_{tot} = sum over all collision cross-sections
ϕ = electric potential

I. Introduction

For the past several years there is a continuous effort to develop Hall thrusters for use in small spacecraft. One of the main obstacles in developing low power Hall thrusters is to accommodate high performance with acceptable life time. In low power operation (50 - 250 W), the propellant mass flow rate is reduced, which leads to poor propellant utilization efficiency. Conventional solutions for scaling towards low power require a small diameter channel.[1] However, due to ion sputtering, thinner dielectric walls reduce significantly the thruster life time. At present, state-of-the-art low power Hall thrusters have an anode efficiency of 20 - 40 % and a life time of 1000 - 3000 hr.[2–7] These parameters are considerably lower than medium powered devices.[8]

The CAMILA concept was developed to improve the performance of low power Hall thrusters.[9] This concept departs from classical design in two ways: (1) the anode is consisted by two concentric electrodes placed parallel to the thruster; (2) additional longitudinal magnetic field is added to protect the anode surfaces. The expected increase in efficiency is based on extending the propellant ionization region inside the anode cavity, whereas the longitudinal magnetic field prevents ions from recombining on the anode surfaces. Considering the CAMILA channel dimensions and wall thickness, which are similar to medium power thrusters, it has an expected life time above 4000 hr. Experimental investigations of the CAMILA thruster have shown improved anode efficiency over classical designs, achieving more than 40 % at 180 W.[8] This improved performance was obtained using relatively weak longitudinal magnetic fields. The simplified one dimensional model for the CAMILA, proposed by Kapulkin,[10] fails to predict the observed improvement in performance.

In this paper we present results from a fully kinetic numerical simulation, which captures the inherently two dimensional character of the discharge. Two separate cases are studied: (1) simplified CAMILA which uses a conventional magnetic circuit (similar to the experimental configuration) with a weak longitudinal field; (2) full CAMILA, which uses an additional magnetic circuit to strengthen the longitudinal component of the magnetic field. The model is described in section II. The results for the simplified and full CAMILA are presented in section III and section IV respectively.

II. Numerical Method

As this work is the first to simulate the CAMILA thruster it was decided not to use fluid or hybrid approximations since they require additional physical assumptions. Instead, a fully kinetic particle-in-cell (PIC) method was selected. In this scheme, particles represent the plasma whereas the electric potential, charge and particle densities are computed on a grid. The plasma dynamics are determined from the boundary conditions and particle-particle interactions. In general, the inter-particle force can be divided into two parts: (1) an averaged force created by long range particle interactions; (2) a rapidly varying force attributed to short range particle interactions, i.e., collisions. The long range force can be represented by the Lorentz force, using localized electric $\vec{E}$ and magnetic $\vec{B}$ fields. The equations of motion are integrated to advance the particles. The collisions are treated as stochastic events, using random numbers to compute collision probabilities. Typically, due to computational restrictions, each macro-particle represents a collection of hundred of thousands of actual particles. Stability criteria require the length of a grid cell to be in the order of the Debye length and the time step is determined accordingly.[11]

The objective of the model is to simulate accurately the plasma inside the anode cavity of the CAMILA Hall thruster. However, solving the three dimensional problem is computationally intensive. The problem can be reduced to two dimensions by neglecting the density and electric field variations in the azimuthal direction while tracking particle velocities in all three dimensions. As Hall thrusters are usually axisymmetric, it is possible with such an approximation to model most features observed experimentally. The anomalous electron transport, which appears due to azimuthal fluctuations, is ignored. Previous fully kinetic PIC simulations of Hall thrusters usually employed computational over-simplifications, e.g., artificial electron to ion mass ratio, artificial vacuum permittivity[12] or geometrical scaling.[13] These ways help to decrease the simulation time but at the cost of changing some aspects of the physical model. In the case of artificial permittivity constant, the whole dynamics of the plasma may change. The Debye and wall sheaths become enlarged and rescaling back to the physical system is impossible. As in this work we model a new type of Hall thruster the detailed variations of the plasma and electrostatic field are important. It was decided not to rescale the problem artificially .

The simulation used in this work was based on the program XOOPIC,[14] a 2d3V PIC-MCC code capable of modeling charged particles in two dimensional space. The original program was modified to properly model the Hall thruster physics. Major changes include the addition of gas dynamics, more advanced particle-boundary interactions and post processing capabilities. The multiprocessor variant of the program was also refined to the specifics of the model and a parallel Poisson solver was added. The program utilizes a null collision MCC for simulating electron-neutral collisions.[15] A Poisson solver (dynamic ADI) is used to solve the electric field self consistently from the charge density, whereas the magnetic field is held constant. The magnetic system was modeled using the program FEMM.[16] The PIC cycle is depicted in Fig. 1 and the important computational phases are described next.

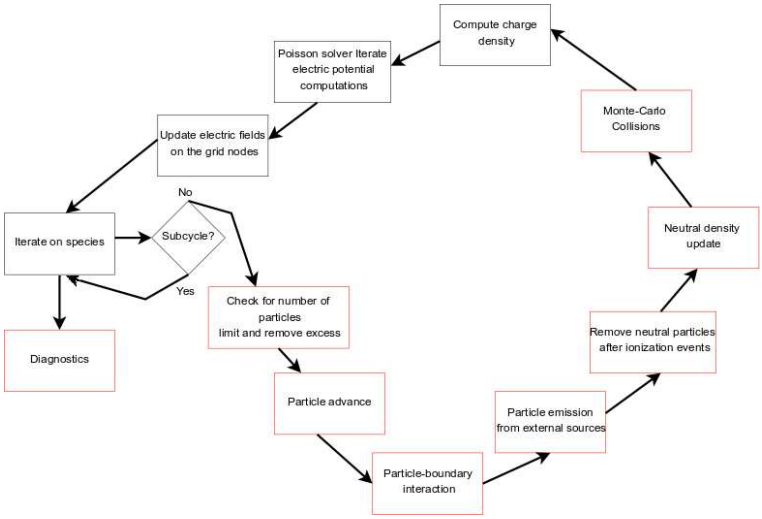

Figure 1: Flow chart of the PIC cycle.

A. Particle Advance

For a non-relativistic particle in an electro-magnetic field, the equation of motion (excluding collisions) is given by two first order differential equations:

$$m_j \frac{d\vec{V}_j}{dt} = q_j \left[\vec{E} + \vec{V}_j \times \vec{B}\right] \tag{1}$$

$$\frac{d\vec{x}_j}{dt} = \vec{V}_j \tag{2}$$

where q_j, m_j, $\vec{x_j}$ and $\vec{V_j}$ are respectively the charge, mass, location and velocity of a specific macro-particle (indexed by j). An efficient second order leap frog method is used to integrate the equations using the Boris rotation method.[17] There are three types of particles in the model: (1) ions with unit positive charge (XeII) ; (2) electrons with unit negative charge; (3) neutrals with zero charge (XeI). The Xenon ions and neutrals have the same mass. The neutral particles, being chargeless, follow constant velocity trajectory - their paths can only be changed by collisions with the walls. In order to reduce computation, a subcycling scheme is used: the heavy species, ions and neutrals, are advanced every 100 and 200 electron time steps respectively.

B. Particle Boundary Interactions

To complete a self consistent model of the plasma it is required to properly model the boundaries. These serve as the physical interface through which energy and particles enter and leave the system. Since we model particles directly, the details of particle-wall collisions need to be attended. Electron-boundary interactions are implemented in XOOPIC with a Vaughan-based model,[18] which includes energy and angular dependence. This model was used for the Boron-Nitride dielectric walls (taken from Ref. 19) assuming that all emitted

electrons are true secondaries. Since electron energy does not exceed 50 eV, the secondary electron emissions from the metal surfaces are ignored.

An important modification made to the original XOOPIC program was the inclusion of heavy species interactions with the boundaries. The parameter of importance, which defines to what extent the reflected particles have their temperature adjusted toward that of the surface, is given by the thermal accommodation coefficient:

$$a_c = (F_i - F_r)/(F_i - F_w) \tag{3}$$

where F_i and F_r are the energy fluxes of the incident and reflected particle, F_w is the energy flux of the reflected particle assuming full accommodation. We added diffusive reflection ($a_c = 1$) for the neutral particles and recombination-reflection with partial accommodation for ions ($a_c = 0.8$). In the first case, the incident particle is re-emitted according to half Maxwellian distribution at the wall temperature (700 K), with the velocity oriented at random direction. In the second case, information about the incident particle velocity is used to calculate the velocity of the reflected neutral.[20]

In order to model the cathode, a new type of boundary was introduced - the free space (FS) boundary. This boundary emits (inserts) electrons according to half-Maxwellian velocity distribution (with temperature of 10 eV). Initially it ignites the discharge by emitting a constant electron current of 0.1 A. Once the ion current on the FS boundary exceeds 0.1 A, the electron emission is regulated automatically to maintain quasi-neutrality near its surface (a similar method was used in Ref. 12). Electrons and heavy species that cross this boundary are deleted from the simulation. The gas distributor is also modeled as a particle source, an emitter with a fixed mass flow rate located on the back plate. The Xenon atoms are emitted using half-Maxwellian distribution at a temperature of 300 K.

C. Electron-Neutral Interactions

The most important (frequent) type of particle-particle collision inside the Hall thruster discharge are between electrons and neutrals. Considering only large angle binary collisions (weakly ionized plasma), a two particle collisional frequency is used for the model. At the start of simulation the maximal collision frequency is computed by:

$$\nu_{max} = max(n_a) max[\sigma_{tot}(\varepsilon) V_e] \tag{4}$$

and the null probability is obtained by:

$$P_{null} = 1 - exp(-\nu_{max} \Delta t) \tag{5}$$

where σ_{tot} is the sum over all collision cross-sections, V_e is the electron speed, Δt is the electron time step, ε is the particle energy and n_a is the neutral gas density. The maximum number of macro-particle collisions is then:

$$N_c = N_e P_{null} \tag{6}$$

where N_e is the total number of electron macro-particles in the computational region. Every electron time step this number of randomly selected macro-particles is tested for three types of collisions: elastic, excitation and ionization. In contrast to the original algorithm in XOOPIC, which assumed a fixed gas density, the collision frequency of each collision type is computed according to the local density of the gas in the electron's location (resolved to center of grid cells). The collision type is determined using a random number. The electron-Xenon cross sections used for the simulation are adopted from Refs. 21 and 22. In the case of elastic collision, the incident electron scatters after the collision but does not lose energy. In collisional excitation, the incident electron losses 8.3 eV and scatters, whereas the excited neutral is assumed to instantly decay to its fundamental state. In collisional ionization, the incident (primary) electron losses 12.1 eV and scatters. The remaining energy is partitioned between the primary and the newly created secondary electron. The ion velocity is determined from Maxwellian distribution at the gas temperature. In addition to the creation of ions, the excess neutrals are removed from the simulation to conserve mass. This process was added to the original XOOPIC program in order to follow changes in the neutral density. Since the neutral density is important for the evaluation of the collision frequency, it is updated every electron step. However, the excess neutrals are removed only at the neutrals time step.

D. Field Solver

Generally, solving an electromagnetic problem requires solution of Maxwell equations. However, in the present work an electrostatic approximation is employed in order to reduce the computational burden. Hence, only the Poisson equation is dynamically solved and the external magnetic field is unaffected by the charged particle dynamics. This approximation is justified by the fact that the current in the low power Hall thruster is sufficiently small and does not substantially alter the external magnetic field. Defining the electric potential as $\vec{E} = -\nabla\phi$ we obtain from Gauss equation the Poisson equation:

$$\nabla^2\phi = -\frac{\rho}{\epsilon} \tag{7}$$

where ρ is the charge density and ϵ is dielectric permittivity. In order to discritize Eq. (7) over the computational space, a two-dimensional NGP (nearest grid point) method is used on a uniform rectilinear grid. The charge density is found by a bi-linear interpolation of the charge from each particle to the computational grid nodes.

The solution of the electrostatic potential is divided into two parts. First, a fixed Laplace solution ($\rho = 0$) is obtained for a given electrostatic boundary conditions. Second, a solution of the Poisson equation (assuming 0 V on the boundaries) is obtained in each iteration, including both space charge and surface charge on dielectrics. The electric field is computed by superposition of both solutions. The main cost of computation is divided between the particle push and the Poisson solver. In the present work, parallel processing was implemented to reduce computational time. The original ADI solver was paralleled using a Schwarz alternating method, similarly to the work in Ref. 23. In this technique, information regrading the overlapping buffer region is passed between neighboring processors. Each processor uses this extra information to obtain the potential in its region. The solution across the overlapping domain is transferred from each processor to its counterparts. This process is repeated until converged solution is obtained. Tests have shown discrepancy of less than 1 % between serial and parallel solutions.

E. Electrostatic Boundary Conditions

The electrostatic boundary conditions for the model were chosen to resemble the actual thruster geometry and electrical circuit, as shown in Fig. 2. The Dirichlet boundary conditions imposed on the model are 300 V on the 34 mm long anode surfaces and 0 V on the free space boundary (right boundary in Fig. 2). The potential on the back plate was chosen as 200 V. This value was selected as a zero order approximation for a floating conductor. On the dielectric walls (17 mm in length), Neumann boundary conditions are enforced with the normal electric field component set to zero. In addition, the dielectric walls accumulate charge locally thus having a floating potential. The magnetic field in the simulation is constant and is provided as an external input.

F. Gas Initial Conditions

In order to obtain the initial state of the gas distribution, a preliminary simulation of gas flow was conducted. This computation ran until the mass flow rate at the free space boundary reached a steady state. To reduce simulation run time, electrons were not introduced and a large time step was used. In addition, numerical experiments showed that starting the full simulation from this steady state cause an abrupt increase in plasma generation. The high density plasma created large numerical heating, which eventually caused the simulation to collapse. To prevent this behavior the initial state of neutrals was carefully adjusted hence the maximum plasma density did not exceed the simulations limit.

G. Numerical Parameters

We evaluate the numerical parameters required for the simulation by first selecting the Xenon mass flow rate. A value of 0.55 mg/s was used as a compromise between the expected power level and available computational resources. In such a case, the plasma density is $n_e \approx 1.5e17$ m^{-3}, assuming full ionization and uniform distribution. Using this density and a typical plasma temperature of 15 eV the Debye radius is determined as $\lambda_D \approx 8e-5$ m. The simulation domain conforms to actual thruster dimensions with an axial length of 51 mm, and a radial length of 12 mm. Using a grid cell length of λ_D the size of the computational grid was chosen as 1000 $\times$ 150 cells divided into 4 blocks (250 $\times$ 150), each allocated to a different CPU.

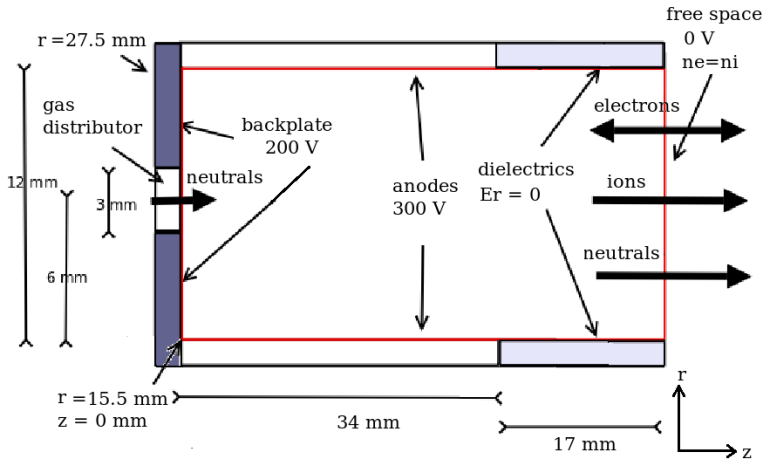

Figure 2: The CAMILA model boundary conditions and the computational region - marked by the red lines.

The simulation electron time step is determined as $\Delta t \approx 1e-11$ s. The number of computer macro-particles in each cell needs to be large enough to maintain low level of fluctuations, but not prohibitively large, as the computational time scales linearly with the number of macro-particles. In order for the electron-XeI collisions to dominate the number of macro-particles has to be on the order of several hundred.[24] Using these estimates, a total of $\sim$ 30 million macro-particles are required; however, particle distribution is uneven thus reducing the required number of macro-particles. In the current model $\sim$ 10 million macro-particles per species are used.

III. Simulation Results - Simplified CAMILA

Originally, in CAMILA, a spacial magnetic circuitry (anode coils in our model) is required to strengthen the longitudinal component of the magnetic field. However, it was discovered in experiments that even without the additional magnetic circuitry, improved anode efficiencies were obtained. In order to understand the mechanisms involved in the improved performance, a simulation with similar magnetic configuration (as in the experiments) was tested and its results are presented in this section.

The simulation ran for 140 μs with real computation time of about 4 months (14 million program iterations). The convergence of the simulation for a mass flow rate of 0.55 mg/s is demonstrated by the time dependent behavior of the discharge current, shown in Fig. 3. Due to the initial high neutral density, plasma generation is higher than the steady state value. However, when the excess neutrals are ionized the currents are reduced. There is no exact steady state, instead, oscillations with large amplitude modulations are present, with frequencies of 10 - 20 kHz . These oscillations were observed in classical thrusters as well and are refereed to as Breathing mode (for example see the review in Ref. 25); they arise from the neutral depletion dynamics. From Fig. 3, it can also be seen that the FS ion current is nearly equal to the discharge current. Usually, it is expected that the discharge current exceeds the FS ion current. However, in this work, azimuthal waves that induce higher conductivity are not modeled. The electron currents collected by the inner and outer anode are presented in Fig. 4, the total collected ion current is shown as well. The inner anode collects much larger electron current than the outer anode (ratio of $\sim$ 7/1). This is expected since the magnetic lines of force intersect the inner anode but not the outer anode. The anode efficiency is evaluated as $\sim$ 31% at 63 W. Variations of plasma parameters along the axial direction (averaged along the radial direction) are shown in Fig. 5. We can observe that the the plasma density reaches a maximum few millimeters outside the anode cavity. The density sharply falls inside the cavity but significant penetration of plasma is present. The ionization rate, shown in Fig. 5, is evaluated using the average velocity in each cell as:

$$R = n_a n < Q_{eai} V_e > \tag{8}$$

where n is the plasma density and $< Q_{eai} V_e >$ is the ionization reaction rate .We note that the maximum density correlates with the maximum ionization rate. The presence of electric field in this maximum is also indicated by the fact that the electric potential maximum is found upstream, inside the anode cavity.

The penetration of plasma inside the anode cavity is important because the ionization efficiency depends on the initial ion density. One example is the dependence of the ionization length on the initial plasma density, as developed in Ref. 10. To understand the controlling factors of plasma penetration in our case, several simulations were analyzed at different transient discharge currents and plasma densities, as shown in Fig. 6. The penetration length is measured from the anode-dielectric boundary, found at 34 mm, and is indicated by the knee (largest change) in the density profile. We can observe that the penetration length increases with the ratio of plasma density to discharge current, $\frac{n}{I_d}$. However, at greater plasma densities, an additional ionization region develops inside the anode cavity, increasing the penetration even further. Thus we expect a higher ionization efficiency at higher power levels.

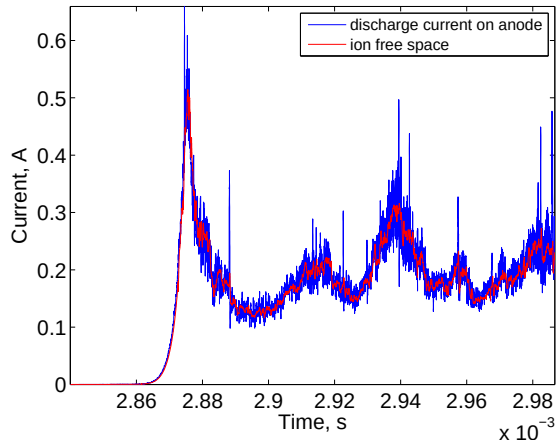

Figure 3: Simplified CAMILA: discharge and FS ion currents versus time.

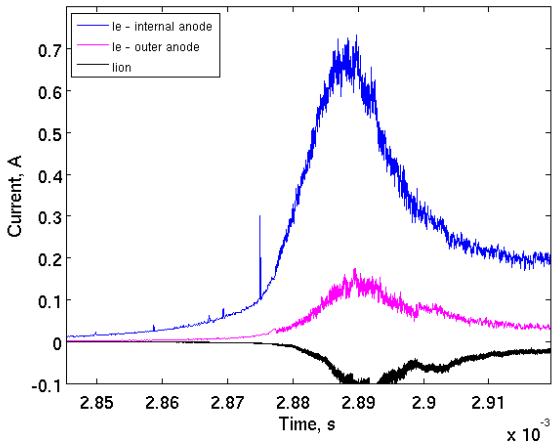

Figure 4: Simplified CAMILA: electron currents collected by inner and outer anodes and the total anode ion current versus time.

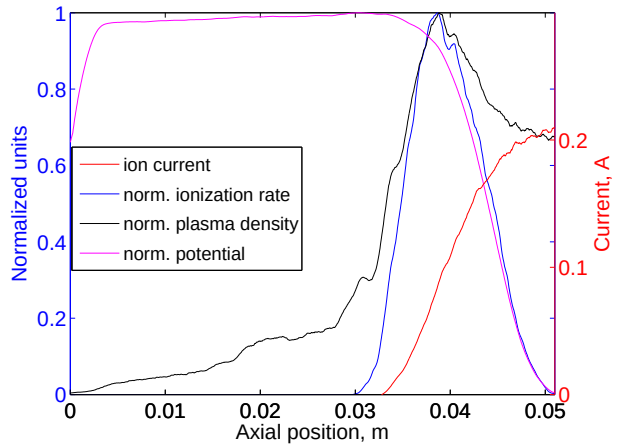

Figure 5: Simplified CAMILA: radially averaged discharge parameters along the axial position

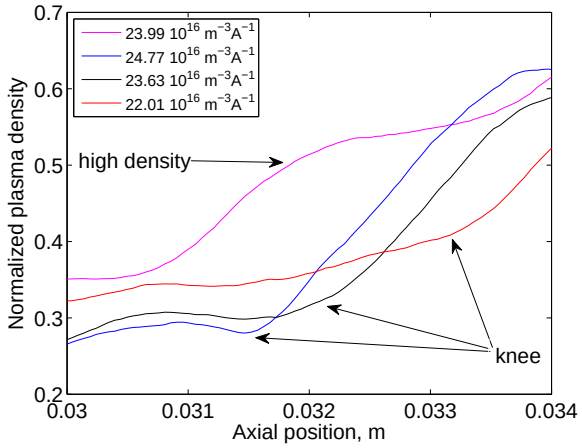

Figure 6: Simplified CAMILA: penetration length, designated as the knee - region of the largest change in density, at different $\frac{n}{I_d}$ ratios.

A. Two Dimensional Effects

The following section presents an analysis of spatial distributions of various plasma parameters in the simplified CAMILA model. The distribution of the electric potential near the anode-dielectric boundary is shown in Fig. 7. The most distinct feature is the concave electric equipotential lines near the anode-dielectric boundary. These contours are created due to the penetration of plasma inside the anode cavity. The increased electron conductivity along the magnetic line of force allows the electrons to escape to the anodes. As a consequence, the slower ions form a net positive potential that keep them in place, creating a higher-than-anode-potential inside the cavity. A similar electron repelling region was found near the anode of classical thrusters.[26,27] However, in the CAMILA channel, due to the the placement of the anodes, once a higher-than-anode-potential is created inside the cavity, a focusing profile is automatically established in direction of the falling electric potential (as equipotential lines do not cross).

The cell averaged plasma density and the ionization rate distributions are shown in Fig. 8 and Fig. 9 respectively. We observe that the constant-density lines follow closely the magnetic lines of force. The magnetic pressure near the outer anode concentrates the plasma toward the inner anode while the outer anode is kept isolated. The ionization rate closely matches the Hall parameter distribution shown in Fig. 10. The Hall parameter is computed by averaging, in each cell, the ratio between the perpendicular and the parallel components of the electron velocity relative to the magnetic field $\left|\frac{V_{e\theta}}{V_{e\perp}}\right|$; values vary considerably between 10 - 1000. The classical transport theory predicts Hall parameter values of several hundred, however, reduced values are found in the dielectric portion of the channel. This phenomenon can be explained by a near-wall conduction, i.e., electrons near the wall are able to travel along the wall due to collisions with the dielectric surface. In turn, they are free to move along the entire magnetic line of force on which they are found. The cooling effect of the walls can be seen in Fig. 11, indicating the cell-averaged electron energy. In Fig. 12, we directly observe the two-dimensional cell-averaged trajectories of the ions as they accelerate along the channel. We notice that the majority of ions is directed in the axial direction with the beam located off-center, closer to the inner anode.

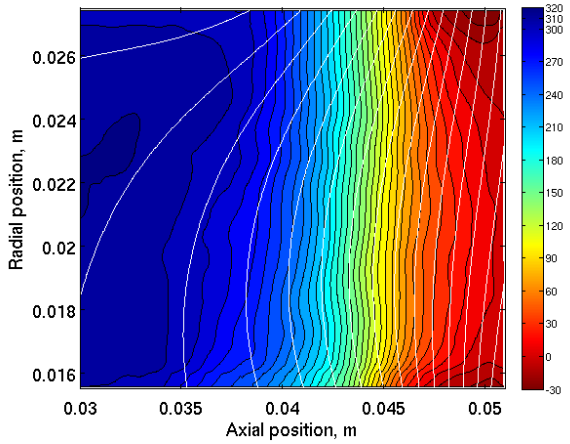

Figure 7: Simplified CAMILA: spatial distribution of electric potential contours - color coded, V. White lines are magnetic force lines.

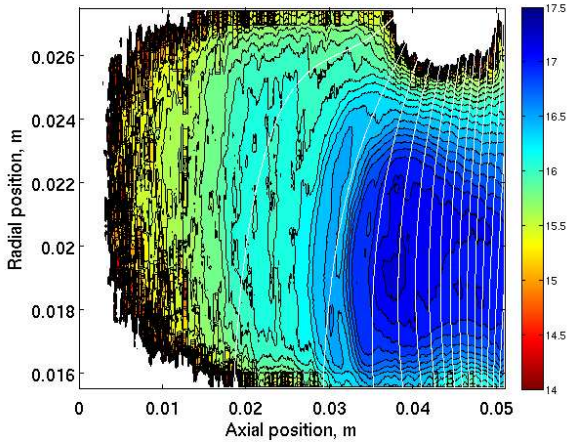

Figure 8: Simplified CAMILA: spatial distribution of ion density contours - color coded log scale, m^{-3}. White lines are magnetic force lines.

B. Particle Trajectories

The strength of the PIC method lies in its ability to model the kinetic effects. In order to validate the cell averaged results we observe a sample of individual trajectories of both electrons and ions (macro-particles). Figure 13 depicts the trajectories projected on the two dimensional plane. We can separate the motion of electrons to three distinct cases: (1) strong magnetic field - the electrons are locked around the magnetic lines of force ; (2) large magnetic gradient (high to weak) - the electrons move in "banana" shaped trajectories and are able to travel many Larmor radii (this effect is known in the literature as neoclassical transport[28]);

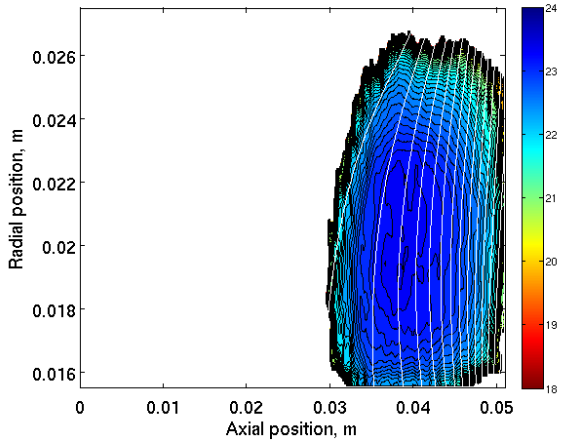

Figure 9: Simplified CAMILA: spatial distribution of cell-averaged ionization rate contours - color coded log scale, $m^{-3}s^{-1}$. White lines are magnetic force lines.

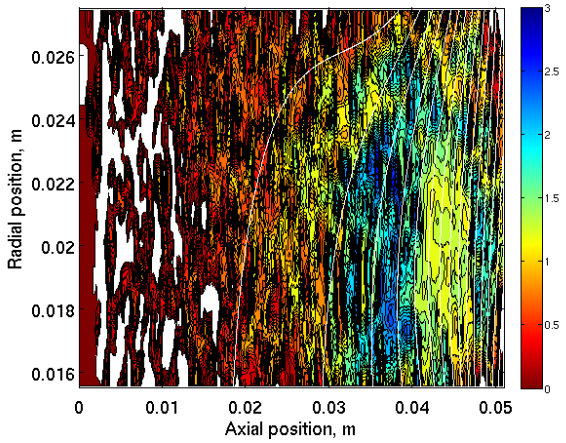

Figure 10: Simplified CAMILA: spatial distribution of cell-averaged Hall parameter contours - color coded log scale. White lines are magnetic force lines.

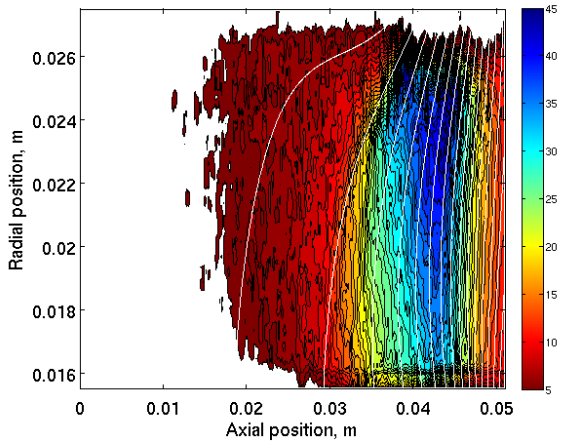

Figure 11: Simplified CAMILA: spatial distribution of cell-averaged electron energy contours - color coded, eV. White lines are magnetic force lines.

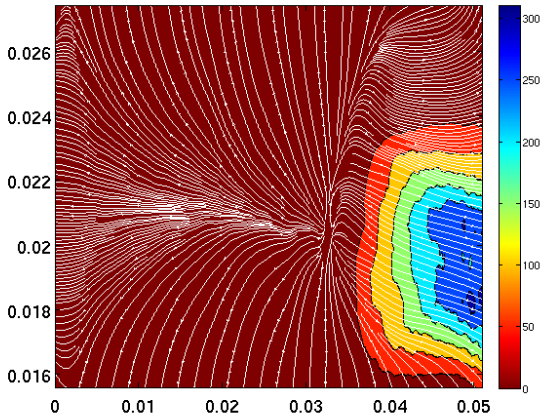

Figure 12: Simplified CAMILA: spatial distribution of cell-averaged ion current density contours - color coded, A/m^2. White lines are ion trajectories.

(3) weak magnetic field - the electrons are completely unconfined. The ion particle motion, shown in Fig. 14, is less complicated and follows the fluid streamlines.

IV. Simulation Results - Full CAMILA

In the full CAMILA magnetic configuration, the longitudinal component of the magnetic field, parallel to the anodes, is greatly enhanced. For this simulation, the longitudinal magnetic circuit was selected according to the requirement developed in Ref. 10. This requirement specifies the minimum magnetic field strength inside the anode cavity, which is needed to retard ion motion toward the anodes while heating the electrons inside the cavity. The model in Ref. 10, however, disregards the characteristic minimum that is always created as a byproduct of the complex magnetic field. This minimum can potentially cause the creation of an electrostatic barrier which, in turn, will increase ion flux to the walls. The simulation analysis is aimed to understand these effects. Because of the long time required for the computations, the simulation did not

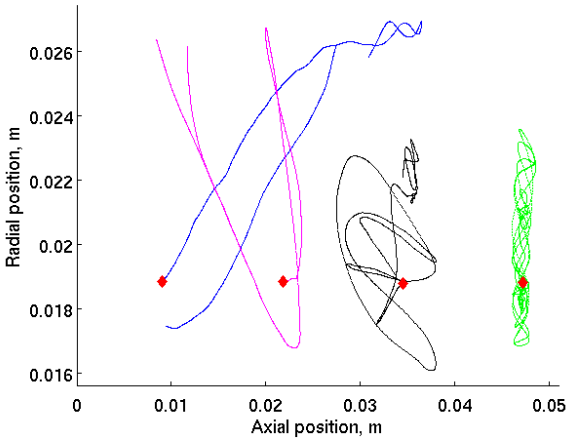

Figure 13: Simplified CAMILA: two dimensional projection of individual electron trajectories. The initial position is marked with a rhombus.

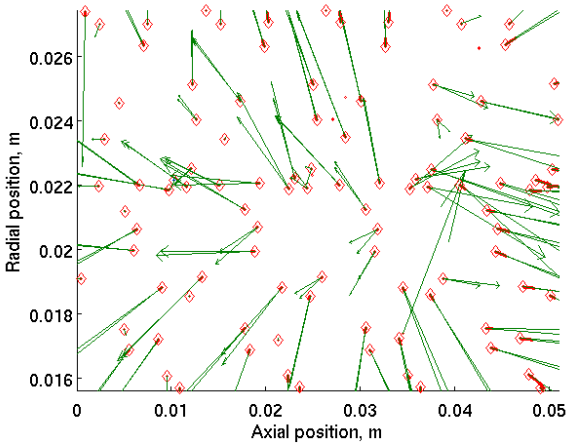

Figure 14: Simplified CAMILA: two dimensional projection of individual ion trajectories and velocity vectors. The initial position is marked with a rhombus.

reached a steady state, however, it is instructive to observe the transitional state (FS ion current of 0.115 A). The simulation used the same mass flow rate and boundary conditions, similarly to the simplified CAMILA model.

The variations along the axis of the main discharge parameters (averaged along the radial direction) are shown in Fig. 15. We observe that no significant potential hump is created; however, the acceleration zone is shorter and closer to the FS boundary. The highest plasma density and ionization rate are inside the anode cavity, with the maximum near the gas distributor, influenced by the high gas density there. The distribution of the ion current is completely different than in the simplified CAMILA case; the axial ion current reaches the maximum before the main ion acceleration zone (the region of the sharpest potential drop) and is slightly reduced towards the FS boundary. The data indicate that there is an ion loss to the dielectric walls. The electron currents collected by the inner and outer anodes and the total collected ion current are shown in Fig. 16. We notice that the ion flow to the anodes has essentially vanished, whereas the electron current ratio between the inner and outer anode is now reversed (ratio of $\sim 1/3$) and is more equally distributed compared to the simplified CAMILA case.

A. Two Dimensional Effects

As shown in Fig. 17, the electric equipotentials are markedly different from the equipotentials obtained in the simplified CAMILA configuration. As predicted by the analytical model in Ref. 10, the electric field inside the anode cavity is now reversed. The anode cavity center line has lower potential than the anodes, with the electric field points away from the anode surfaces. The detailed simulation, however, goes beyond the one dimensional description. The figure shows that near the anodes, where the lines of force intersect with the anodes, the potential is fixed at the anode potential. Electrons found in these regions are free to move along the magnetic lines of force to the anodes. Due to the curved shapes of the magnetic lines of force, the electric potential assumes the shape of an expanding nozzle near the anode-dielectric interface. We also observe that the region of ion acceleration is now compressed toward the FS boundary. The density of plasma is higher than the one obtained in the simplified case and it is located mainly inside the anode cavity, as shown in Fig. 18. The ionization process is now spread along the entire anode cavity as shown in Fig. 19. The near anode regions, however, are almost completely empty of plasma, effectively reducing the anode cavity width. The Hall parameter distribution is shown in Fig. 20. It clearly indicates the effect of the added longitudinal magnetic field. We observed that near the anode-cavity-center-line, the Hall parameter is considerably reduced. It is a consequence of the radial symmetry; where the center line is a region of low radial electric field, hence lower azimuthal drift velocity is received. The electron energy spatial distribution presented in Fig. 21 shows that electrons are heated evenly along the entire anode cavity with energy > 20

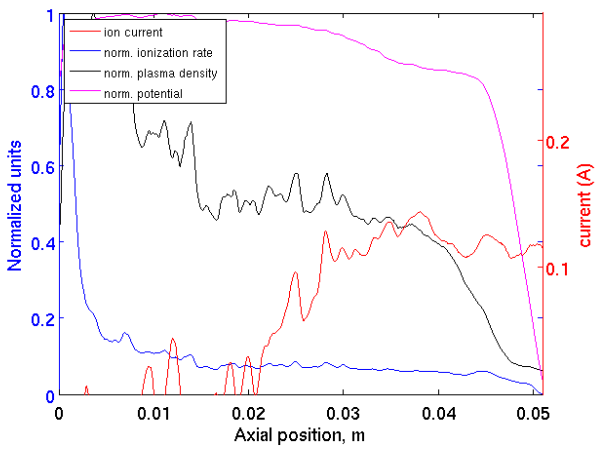

Figure 15: Full CAMILA: radially averaged discharge parameters along the axial position

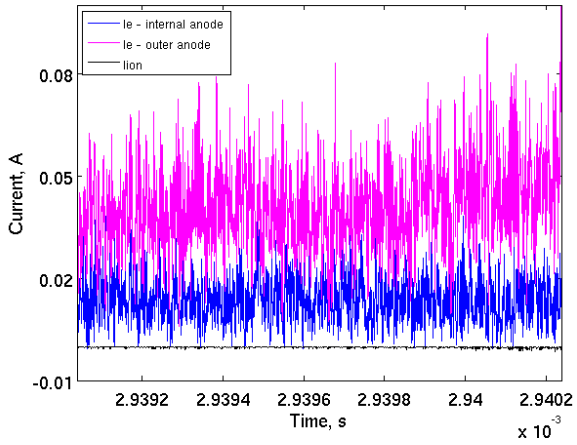

Figure 16: Full CAMILA: electron currents collected by inner and outer anodes and the total anode ion current versus time.

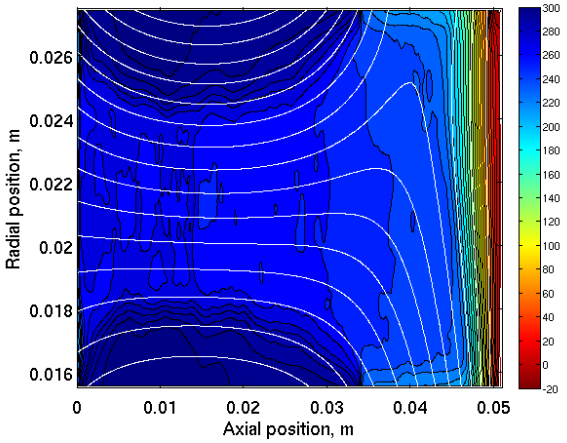

Figure 17: Full CAMILA: spatial distribution of electric potential contours - color coded, V. White lines are magnetic force lines.

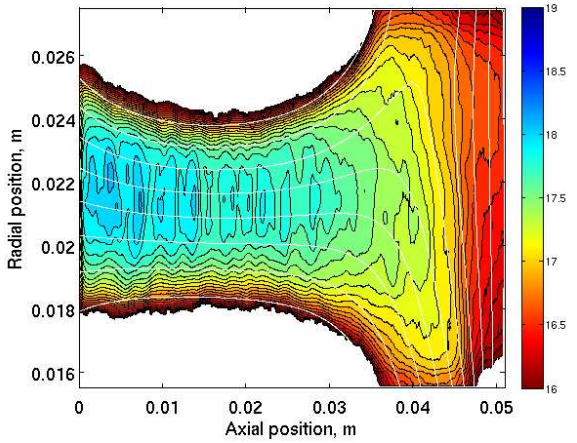

Figure 18: Full CAMILA: spatial distribution of ion density contours - color coded log scale, m^{-3}. White lines are magnetic force lines.

eV, sufficient for effective ionization. This result supports the validity of the analytical model in Ref. 10; however, the near anode regions are populated with low energy electrons. The ion trajectories are shown in Fig. 22. There are two distinct populations of ions: (1) ions generated near the back plate that move toward it and represent pure loss; (2) ions generated at the second half of the anode cavity that accelerate out from the cavity. The ions that escape the anode cavity are not as well focused as in the simplified case and significant ion current is lost to the dielectric walls.

B. Particle Trajectories

In order to complete the analysis of the full CAMILA case we present the typical electron and ion trajectories in Fig. 23 and Fig. 24, respectively. The electrons are magnetized in the entire volume; however, two distinct regions exist: (1) inside the anode cavity where electrons are free to move axially; (2) outside the anode cavity where electrons are free to move radially. The ion motion is determined from the initial position; upstream, the ions move toward the back plate; downstream, the ions move toward the FS boundary. In addition, ions located near the center line of the anode cavity (where the plasma density is highest) are

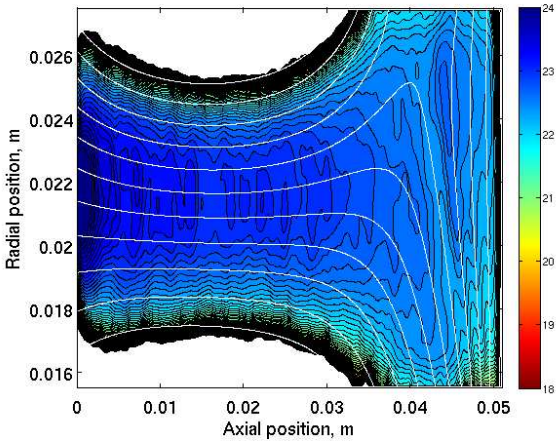

Figure 19: Full CAMILA: spatial distribution of cell-averaged ionization rate contours - color coded log scale, $m^{-3}s^{-1}$. White lines are magnetic force lines.

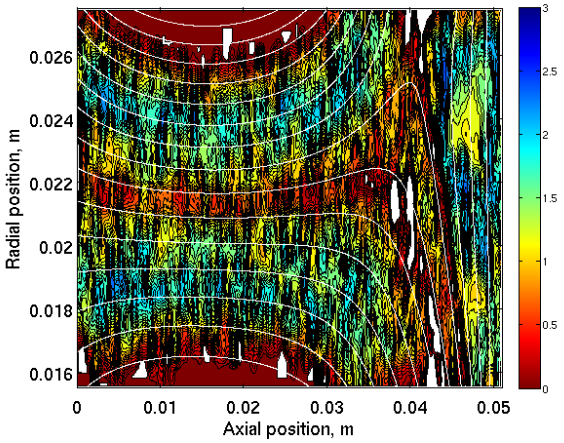

Figure 20: Full CAMILA: spatial distribution of cell-averaged Hall parameter contours - color coded log scale. White lines are magnetic force lines.

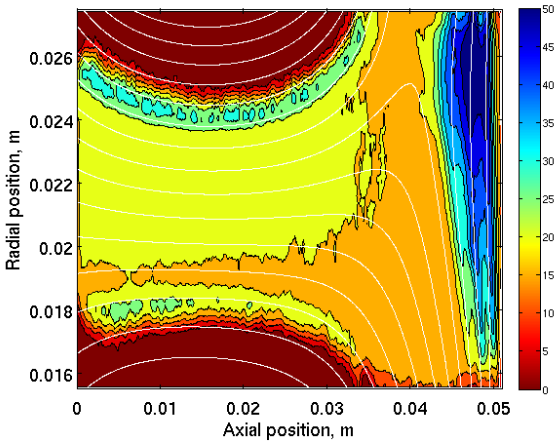

Figure 21: Full CAMILA: spatial distribution of cell-averaged electron energy contours - color coded, eV. White lines are magnetic force lines.

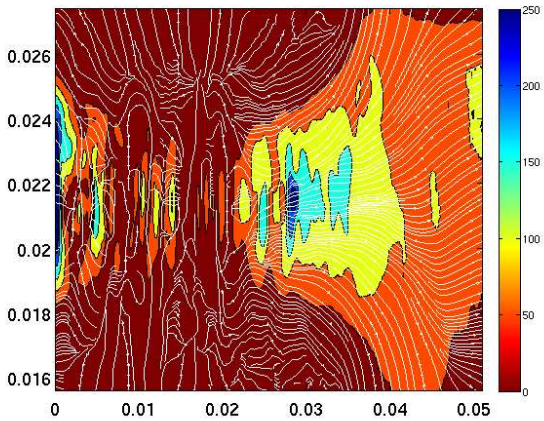

Figure 22: Full CAMILA: spatial distribution of cell-averaged ion current density contours - color coded, A/m^2. White lines are ion trajectories.

confined to that region. Their velocities point toward the center line; near the center the ion velocities are low, however, as the radial distance increases so is the particle velocity. Outside the anode region, ions flow according to the streamlines shown previously (in Fig. 22).

V. Conclusion

Using results from two dimensional PIC simulations, we have analyzed, two configurations of the CAMILA Hall thruster concept. The simplified CAMILA was successfully simulated reaching a state state. The main feature enabling improved efficiency over classical low-power-Hall-thrusters is the focusing potential profile. It is created due to the placement of the anodes, the penetration of plasma inside the anode cavity and the shape of magnetic field. In addition, the penetration of plasma inside the anode cavity improves the overall ionization efficiency. It was noted that the discharge is not symmetric and is attached to inner wall, thus it is possible to find a better magnetic field configuration to centralize the discharge and reduce the ion loss to

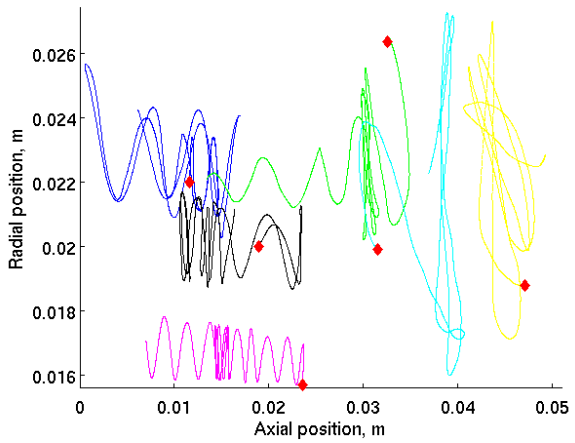

Figure 23: Full CAMILA: two dimensional projection of individual electron trajectories. The initial position is marked with a rhombus.

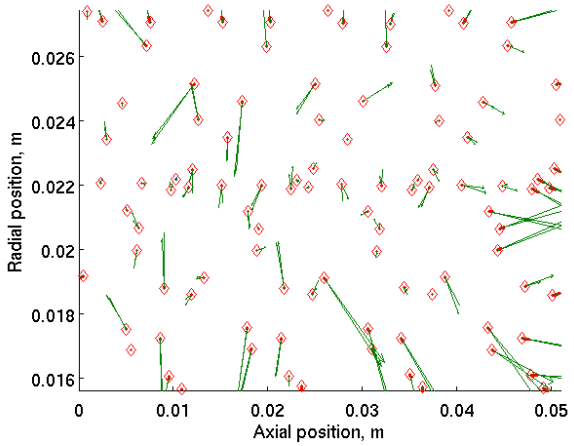

Figure 24: Full CAMILA: two dimensional projection of individual ion trajectories and velocity vectors. The initial position is marked with a rhombus.

the walls. For the full CAMILA configuration, the discharge is markedly different from the simplified case. By enhancing the longitudinal component of the magnetic field, two regions of high electric resistivity are created inside the anode cavity. These regions enable the generation of plasma while retarding ion motion toward the anodes; thus allowing for improved ionization efficiency over the simplified case. However, not all the cavity is utilized since the regions near the anode surfaces, where the magnetic force line intersect, are at lower electron temperature. In addition, this configuration is not sufficient to prevent ion flux to the dielectric walls and back plate.

References

[1]Ahedo, E., and Gallardo, J. M., "Scaling Down Hall Thrusters," *The 28th International Electric Propulsion Conference*, Toulouse, France, March 17 - 21, 2003, IEPC-2003-104.

[2]Hruby, V., Monheiser, J., Pote, B., Rostler, P., Kolencik, J., and Freeman, C., "Development of Low Power Hall Thrusters," *30th AIAA Plasmadynamics and Lasers Conference*, Norfolk, VA, June 28 - July 1, 1999, AIAA-1999-3535.

[3]Raitses, Y., Smirnov, A., Granstedt, E., and Fisch, N. J., "Overrun Discharge Current Operation of Low Power Cylindrical Hall Thrusters," *The 30th International Electric Propulsion Conference*, Florence, Italy, September 17 - 20, 2007, IEPC-2007-222.

[4]Belikov, M. B., Gorshkov, O. A., Dyshlyuk, E. N., Lovtzov, A. S., and Shagayda , A. A., "Development of Low-Power Hall Thruster with Lifetime up to 3000 Hours," *The 30th International Electric Propulsion Conference*, Florence, Italy, September 17 - 20, 2007, IEPC-2007-129.

[5]Loyan, A. V., Maksymenko, T. A., "Performance Investigation of SPT-20M Low Power Hall Effect Thruster," *The 30th International Electric Propulsion Conference*, Florence, Italy, September 17 - 20, 2007, IEPC-2007-100.

[6]Bugrova, A. I., Desiatskov, A. D., Kaufman, H. R., Kharchevnikov, V. K., Morozov, A. I., Zhurin, V. V., "An Improved Small Closed Drift Thruster with Both Conducting and Dielectric Channels," *The 28th International Electric Propulsion Conference*, Toulouse, France, March 17 - 21, 2003, IEPC-2003-263.

[7]Ashkenazy, J., Shitrit, S., and Appelbaum, G., "Hall Thruster Modification for Reduced Power Operation," *The 29th International Electric Propulsion Conference*, Princeton University, NJ, October 31 - November 4, 2005, IEPC-2005-080.

[8]Bober, A. S., and Maslennikov, N., "SPT in Russia- New achievements," *The 24th International Electric Propulsion Conference*, Moscow, September 19 - 23, 1995, IEPC-95-06.

[9]Guelman, M., Kapulkin, A., Balabanov, V., Rabinovich, L., Appelbaum, G., "A New Low-Power Hall Thruster Concept," *The 59th International Astronautical Congress*, Glasgow, Scotland, September 29 -

October 3, 2008, IAC-08-C4.4.6.

[10]Kapulkin, A., and Guelman, M.,"Theoretical Modeling of Ionization Processes in Anode Cavity of CAMILA Hall Thruster," *The 31th International Electric Propulsion Conference*, Ann Arbor, MI, September 20 - 24, 2009, IEPC-2009-068.

[11]Birdsall, C. K., "Particle-In-Cell Charged-Particle Simulations, Plus Monte Carlo Collisions with Neutral Atoms, PIC-MCC," *IEEE Transactions on Plasma Science*, Vol. 19, No. 2, 1991, pp. 65, 85.

[12]Szabo, J., "Fully Kinetic Numerical Modeling of a Plasma Thruster," Ph.D. Dissertation, Aeronautics and Astronautics Dept., Massachusetts Institute of Technology, MA, 2001.

[13]F. Taccogna, S. Longo, M. Capitelli, and R. Schneider, "Plasma Flow in a Hall Thruster," *Physics of Plasmas*," Vol. 12, 2005, pp. 043502.

[14]Verboncoeur, J. P., Langdon A. B., and Gladd, N. T., "An Object-Oriented Electromagnetic PIC Code," *Computer Physics Communications*, Vol. 87, 11 May 1995, pp. 199, 211.

[15]Vahedi, V., and Surendra, M., "A Monte Carlo Collision Model for the Particle-In-Cell Method: Applications to Argon and Oxygen Discharges," *Computer Physics Communications*, Vol. 87, 2 May 1995, pp. 179, 198.

[16]Meeker, D. C., Finite Element Method Magnetic, Software Package, Ver. 4.0.1, URL:http://www.femm.info, 2010.

[17] Birdsall, C. K., and Langdon, A.B., *Plasma Physics via Computer Simulation*, Adam Hilger, Bristol, 1991, Chap. 4.

[18]Vaughan, J. R., "A New Formula for Secondary Emission Yield,"*Electron Devices, IEEE Transactions on*, Vol. 36, 2002, pp. 1963, 1967.

[19]Dunaevsky, A., Raitses, Y., and Fisch, N. J., "Secondary Electron Emission from Dielectric Materials of a Hall Thruster with Segmented Electrodes," *Physics of Plasmas*, Vol. 10, 2003, pp. 2574.

[20] Bird, G.A., *Molecular gas dynamics and the direct simulation of gas flows*, Clarendon Press Oxford, New York, 1994, Chap. 5.

[21]Rejoub, R., Lindsay, B. G., and Stebbings, R. F., "Determination of the Absolute Partial and Total Cross Sections for Electron-Impact Ionization of the Rare Gases", *Physical Review A*, Vol. 65, 2002, pp. 42713.

[22]Ishimaru, Y., and Shimozuma, M., "Electron Collision Processes in Gaseous Xenon", *Nuclear Instruments and Methods in Physics Research Section B: Beam Interactions with Materials and Atoms*, Vol. 207, 2003, pp. 373, 380.

[23]Sudhakar M., and James, A. M., "Ion Engine Discharge Chamber Plasma Modeling Using a 2-D PIC Simulation," *42nd Joint Propulsion Conference and Exhibit*, Sacramento, CA, July 9 - 12, 2006, AIAA 2006-4488.

[24]Hockney, R. W., and Eastwood, J. W., *Computer Simulation Using Particles*, Adam Hilger, Bristol and New York, 1988, Chap. 9.

[25]Choueiri, E. Y., "Plasma Oscillations in Hall Thrusters," *Physics of Plasmas*, Vol. 8, No. 4, 2001, pp. 1411, 1426.

[26]Keidar, M., Boyd, I., and Beilis, I., "Analyses of the Anode Region of a Hall Thruster Channel," *38th Joint Propulsion Conference and Exhibit*, Reston, VA, July 8 - 10, 2002, AIAA 2002-4107.

[27]Dorf, L., Semenov, Raitses, Y., and Fisch, N. J.,"Electrostatic Probe Apparatus for Measurements in the Near-Anode Region of Hall Thrusters," *Review of Scientific Instruments*, Vol. 75, No. 5, 2004, pp. 1255, 1260.

[28]Chen, F. F., *Introduction to Plasma Physics and Controlled Fusion. Volume 1: Plasma Physics*, 2nd ed., Plenum Press, New York, 1984, Chap. 5.